Journal of Alloys and Compounds 1026 (2025) 180339

Contents lists available at ScienceDirect

Journal of Alloys and Compounds

journal homepage: www.elsevier.com/locate/jalcom

Laser processing of a CuTiZr-based alloy by powder bed fusion: From bulk metallic glass to metallic glass composite

Aleksandr M. Filimonov [a,c,*], K.M. Saiful Alam [a], Askar R. Kvaratskheliya [a,c], Tim Grieb [b], Binkal Kumar Sharma [c], Bruno Bianchini [c,d], Rafael Formenton Macedo dos Santos [c,d], Leonardo Fernandes Gomes [c,d], Andreas Rosenauer [b], Piter Gargarella [d,e,f], Nattamon Suwannaharn [g], Taisuke T. Sasaki [g], Lutz Mädler [a,c], Ilya V. Okulov [a,c]

[a] Faculty of Production Engineering, University of Bremen, Badgasteiner Str. 1, Bremen 28359, Germany
[b] Faculty of Physics/Electrical Engineering, University of Bremen, Badgasteiner Str. 1, Bremen 28359, Germany
[c] Leibniz Institute for Materials Engineering–IWT, Badgasteiner Str. 3, Bremen 28359, Germany
[d] Graduate Program in Materials Science and Engineering, Federal University of São Carlos, Rod. Washington Luís km 235, São Carlos, SP 13565-905, Brazil
[e] Department of Materials Engineering, Federal University of São Carlos, Rod. Washington Luís km 235, São Carlos, SP 13565-905, Brazil
[f] Center of Characterization and Development of Materials, Federal University of São Carlos, Rod. Washington Luís km 235, São Carlos, SP 13565-905, Brazil
[g] Research Center for Magnetic and Spintronic Materials, National Institute for Materials Science, 1-2-1 Sengen, Tsukuba, Ibaraki 305-0047, Japan

ARTICLE INFO

Keywords:
Laser powder bed fusion
Metallic glass
Glass–crystalline composites
Metastable phase
Structural relaxation

ABSTRACT

Additive manufacturing of bulk metallic glasses using laser powder bed fusion is a challenging task, even for materials with a high glass-forming ability. This is due to the complex thermal history of the additively manufactured glass-forming materials, which are repeatedly heated upon laser processing of subsequent layers, leading to their devitrification. In this study, the influence of laser processing on the commercial Cu-based metallic glass AMLOY-CU01, having a reduced glass transition temperature T_{rg} ~0.44, has been systematically explored, incorporating high-energy synchrotron X-ray diffraction studies complemented by transmission electron microscopy. Despite the low T_{rg}, both vitrified and devitrified states can be obtained. The findings reveal that phase composition is weakly correlated with porosity in the keyhole regime but shows a strong correlation in the lack of fusion regime. The stabilization of the nearly glassy state of the metallic glass is achieved within a laser energy density range of 11 J mm^{-3} $\leq e \leq$ 25 J mm^{-3} and a normalized enthalpy range of 92 $\leq \Delta H \leq$ 239, correlating with moderate porosity values in the obtained samples. The current results provide insights into the fundamental understanding of phase formation in glass-forming materials synthesized by laser processing and pave the way for their engineering application.

1. Introduction

Metallic glass (MG) is a highly supercooled material characterized by a glass transition temperature T_g, below which an energetically unstable non-crystalline state predominates [1–6]. This structural feature provides a solid-like viscosity with superior strength, hardness, and elastic limit of up to 2 % due to the absence of long-range order, making this emerging material attractive for different applications [7–9]. Existing MG fabrication methods, such as casting [10–12], thermoplastic forming [13,14], and melt spinning [15–17], while effective in preserving the glassy state, often face significant limitations with respect to scalability and geometric complexity. However, these challenges inherent to traditional MG fabrication methods have prompted the exploration of advanced manufacturing techniques.

Among these, laser powder bed fusion (L-PBF) has emerged as one of the most widely used additive manufacturing methods [18], offering new possibilities for the fabrication of bulk MG (BMG) [19–25]. It is known that the cooling rates in a small molten pool reach ~10^6–10^7 K s^{-1} [18], which simplifies the synthesis of a glassy structure. MG synthesis can be described by the reduced glass transition temperature $T_{rg} = T_g T_l^{-1}$, where T_g and T_l are the glass transition temperature and the liquidus temperature, respectively [7,26]. Since this criterion is based on the kinetics of crystal nucleation, it has been shown that if $T_{rg} >$ 2/3, the frequency of homogeneous nucleation is negligible. As a result,

* Corresponding author at: Faculty of Production Engineering, University of Bremen, Badgasteiner Str. 1, Bremen 28359, Germany.
E-mail address: filimonov@iwt.uni-bremen.de (A.M. Filimonov).

https://doi.org/10.1016/j.jallcom.2025.180339
Received 6 December 2024; Received in revised form 4 April 2025; Accepted 8 April 2025
Available online 11 April 2025

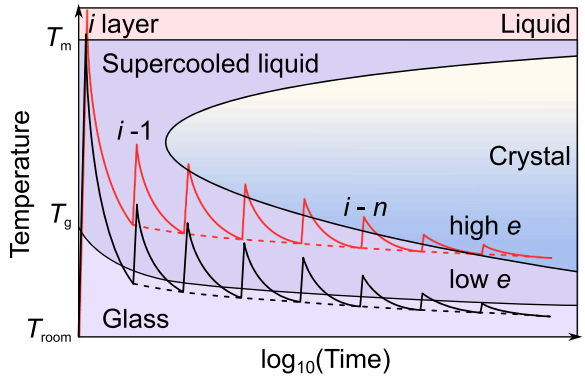

Fig. 1. Schematic illustration of thermal evolution for the cases of (black line) low laser energy density e and (red line) a high e applied across a set of layers during L-PBF. The dashed lines indicate the temperature baseline at the end of cooling for the i layer and the beginning of heating for the $(i-1)$ layer.

the material can be easily vitrified from the liquid state even with cooling rates of $\leq 1\ \mathrm{K\ s^{-1}}$ [7]. Considering the high cooling rates in L-PBF, even for alloys with a high glass-forming ability (GFA) ($T_{rg} > 1/2$), questions remain about the dominance of glass formation over crystallization [27–32]. It was shown that the contribution of thermal effects to the volume fraction of crystals formed should be distinguished on the local and global scales [33]. Specifically, the local scale refers to the heat-affected zone (HAZ), which is constrained by an area proportional to the laser beam, while the global scale refers to the temperature distribution within the entire sample. The dominant contribution of the HAZ to the increase in the volume fraction of crystals occurs when the heat from the current laser track has enough time to fully dissipate before the subsequent track. In other words, the average temperature of the entire material remains below T_g before the new laser exposure [33]. In this case, the high local temperature gradients and cooling rates driven by the laser effectively limit crystal nucleation and, to a certain extent, slow crystal growth in the vicinity of a single track. However, if the temperature stays above T_g before the new laser exposure, the average temperature of the entire material can be increased, eventually leading to an intersection with the nose of the crystalline region (thermal effect on the global scale). The initial temperature of the material before laser exposure can be artificially set. However, over time, it will inevitably be governed by the intrinsic thermophysical properties of the material and the magnitude of the laser exposure. Fig. 1 schematically illustrates the evolution of temperature over time across a set of layers subjected to different laser energy densities (e), also called volumetric energy density (VED) [34,35]. Here $e = P(vht)^{-1}$, where P represents the laser power, v is the scan speed, h is the hatch spacing, and t is the layer thickness. It is assumed that the temperature distribution T near the laser track can be described by the Rosenthal equation [36]. Although the latter incorporates T as a function of P and v, this relation can be roughly rewritten as $T \sim \exp(-e^{-1})$ at constant P. At low e, T remains close to or below T_g (Fig. 1, black line), while at high e, the cooling path can cross the nose of the crystalline region (Fig. 1, red line). The release of absorbed heat from the i layer, treated with a high e, contributes to an increase in the average temperature of the adjacent $(i-1)$ layer.

This interplay between heating, cooling, and the crystallization path highlights the critical role of e in influencing the thermal history and phase results of the material. However, as Hadibeik et al. [37] mentioned, relying solely on the concept of input e to characterize the quality of printed material has inherent limitations. To address this, dimensionless normalized enthalpy ΔH was introduced to account for the coupling between the process parameters and the intrinsic thermophysical properties of the material [38]. Despite the assumption that ΔH complements the concept of e and provides a better quantification of the process regime [37,39–41], especially with respect to the process window for the glassy state, its estimation remains challenging. This is a primary result of the scarcity of data and the need for supporting studies of the thermophysical properties of the material. Furthermore, these thermophysical properties, such as the specific heat capacity c_p or solid density ρ_s, are themselves functions of the process conditions. Kosiba et al. [42] extended the normalized ΔH to include the hatch spacing, which allowed them to successfully select the optimal process window that results in dense components. However, this approach failed to show a stronger correlation with the glassy state. Finally, the question of how to effectively incorporate the scanning strategy into the quantification criteria remains open.

Table 1
The printing parameters.

Parameters	Symbol	Value (s); Δ	Unit
Laser power	P	100–500; 100	W
Scan speed	v	1000–2000; 200	mm s^{-1}
Layer thickness	t	50	μm
Hatch spacing	h	100–200; 50	μm
Oxygen level	–	<100	ppm

Żrodowski et al. [43] showed that high-energy remelting of the previous layer without powder deposition, using a shuffle scanning strategy, helps to reduce material overheating in Zr-based MG. Ye et al. [44] used a pause added between layers of additively manufactured Fe-based MG composite to encourage the cooling of the material, resulting in improved cooling rate efficiency. It was shown that as the distance from the substrate increases, the volume fraction of crystals decreases. Thus, the cooling rate has less influence on the crystal formation than the presence of impurities between the first layer and the substrate. The same conclusion was reached by Sohrabi et al. [45], referring to Pd-based BMG. To exclude the contribution of impurities to crystal formation, Sun et al. [27] tested the influence of a non-crystalline substrate on the synthesis of a multilayer glassy structure, but still obtained a glassy material. They concluded that HAZ is the result of the solid–solid transformation rather than the liquid–solid transformation. Finally, Yang et al. [46] introduced the concept of effective heat shock, which causes the pre-solidified material to undergo crystallization due to the lack of relaxation time in the supercooled liquid.

The current work reports the synthesis of a commercial Cu-based MG, AMLOY-CU01, using L-PBF, followed by systematic phase and microstructural analysis by laboratory X-ray diffraction (XRD) analysis and scanning electron microscopy (SEM). This alloy is chosen because of its limited availability as a commercially produced MG powder and the lack of research on its laser processability. The results obtained confirm that, despite processing the initial glass powder with a low reduced glass transition temperature T_{rg} ~0.44, it is possible to produce a material with a nearly glassy structure without the need for additional pauses or a specialized printing strategy. A comprehensive microstructural analysis, which incorporates synchrotron XRD studies complemented by transmission electron microscopy (TEM), has revealed changes in phase composition driven by the critical role of fine-tuning porosity within a specific e range. Notably, the formation of a crystalline state exhibits a weaker correlation with porosity in the keyhole mode, while demonstrating a stronger correlation in the lack of fusion mode.

2. Experimental methods

2.1. L-PBF sample preparation

The industrial non-crystalline Cu-based powder ($Cu_{45}Ti_{34}Zr_{11}Ni_8Sn_2$ at.%) with $d_{50} = 26.5\ \mu$m, namely AMLOY-CU01, was used as a feedstock for L-PBF (Heraeus GmbH, Hanau, Germany). Three groups of cubic samples (30 pieces per group) with a size of $5 \times 5 \times 5\ \mathrm{mm^3}$ and different printing parameters were manufactured on a Ti–6Al–4V substrate in a protective argon atmosphere using the L-PBF technique

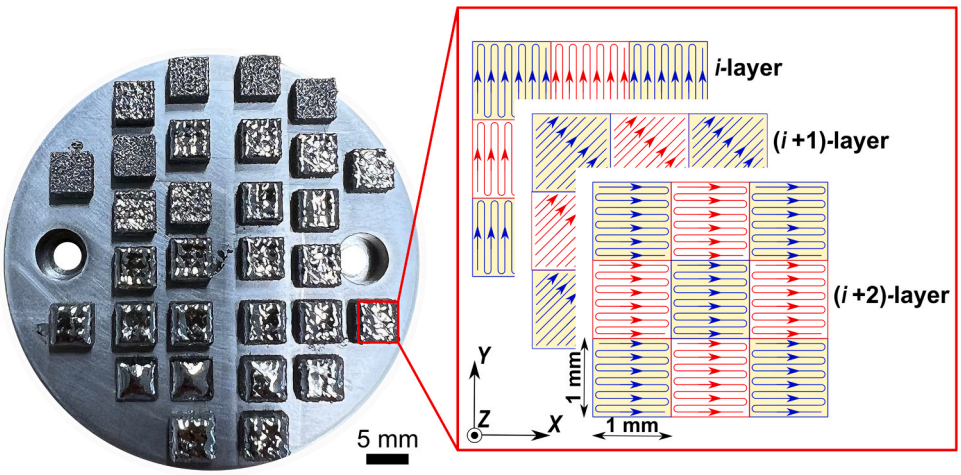

Fig. 2. As-printed samples at $h = 150$ μm with insert sketch of the scanning strategy used for the printing process.

(Table 1). The L-PBF Aconity *MIDI+* printer with an ytterbium fiber laser (700 W, 1070 nm), was used (Aconity3D GmbH, Herzogenrath, Germany). The scan strategy consisted of the chessboard pattern with a unit size of 1 × 1 mm^2 rotated at intervals of 45° in each *x*-*y* plane without pause (Fig. 2). This strategy was chosen because it has been shown to effectively reduce residual stress in Fe-based MG [47]. Because MG synthesis is very sensitive to processing temperature, typical substrate preheating was deliberately excluded but implemented indirectly using a chessboard strategy. Transfer of heat from the scanned cell to the neighboring cells can help to reduce residual stresses in a comparable way [23].

To fabricate the samples for XRD analysis, a 1 mm thick slice was taken from the top side (*x*-*y* plane) of all printed samples using a FANUC MATRA ROBOCUT Alpha α-0iA Robot (FANUC Corporation, Oshinomura, Japan). For SEM analysis, the remaining part of the sample was sliced along (*x*-*z* plane) and across (*x*-*y* plane) the build direction. The sample mounting was performed using a CitoPress-5 machine (Struers, Ballerup, Denmark) and then grounded to 2000-grit SiC via a Tegramin-25 machine (Struers). The final polishing was completed with a suspension of colloidal silica 250 nm (OP-S) (Struers). All polished samples were cleaned by an ultrasonic PALSSONIC PTIC-3-ES bath (Allpax GmbH & Co. KG, Papenburg, Germany) using alcohol and then air-blasted.

2.2. Microstructural and phase characterization

The planar porosity (ϕ) of the normal plane (*x*-*z* plane) was determined using ZEISS Axio Imager.M2m optical microscopy (Carl Zeiss AG, Jena, Germany) and then analysed using the custom Python script.

The sample morphology in both planes was investigated by SEM Supra 40 (Carl Zeiss AG) and the chemical composition was analysed by energy-dispersive X-ray spectroscopy (EDXS) XFlash 6I30 detector (Bruker Corporation, Billerica, USA).

Samples with a thickness of 1 mm were measured using the Brucker D8 Advanced X-Ray diffractometer device (Bruker Corporation, Germany) using CuKα radiation (wavelength is 1.5406 Å). All measurements were performed in continuous scan in the range of 10°–120° 2θ with a step size 0.0149°. The time of exposition for each point ranged from 1 s to 3 s.

To overcome the problem of detecting the fine crystalline phase, the high-energy synchrotron XRD was conducted. To balance experimental feasibility with meaningful data collection, considering time and resource constraints, as well as the large number of samples required to fully cover the entire process window, analyzing all samples was impractical. Therefore, three representative samples with a size of 3 × 2 × 1 mm^3 printed on 8 J mm^{-3}, 20 J mm^{-3} and 48 J mm^{-3} were selected as potential candidates for low, intermediate and high exposure *e*, respectively. Measurements were performed at room temperature, at the German Electron Synchrotron (DESY) PETRA III P02.1 beamline, with a radiation wavelength of 0.2074 Å (energy ~60 keV), spot size at

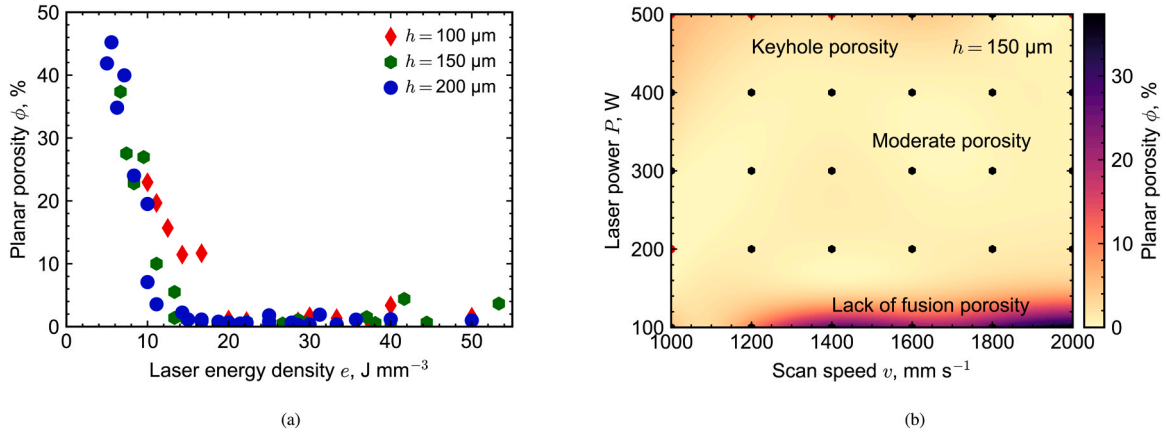

(a) (b)

Fig. 3. Planar porosity ϕ depending on (a) laser energy densities *e* for different hatch spacings *h*, (b) laser powers *P* and scan speeds *v* for $h = 150$ μm. The red exceptions represent empty "porosity" points that are excluded for interpolation. They mean either the complete absence of the sample or/and the absence of a large fragment of the sample. (For interpretation of the references to color in the legend of this figure, see the web version of this manuscript.)

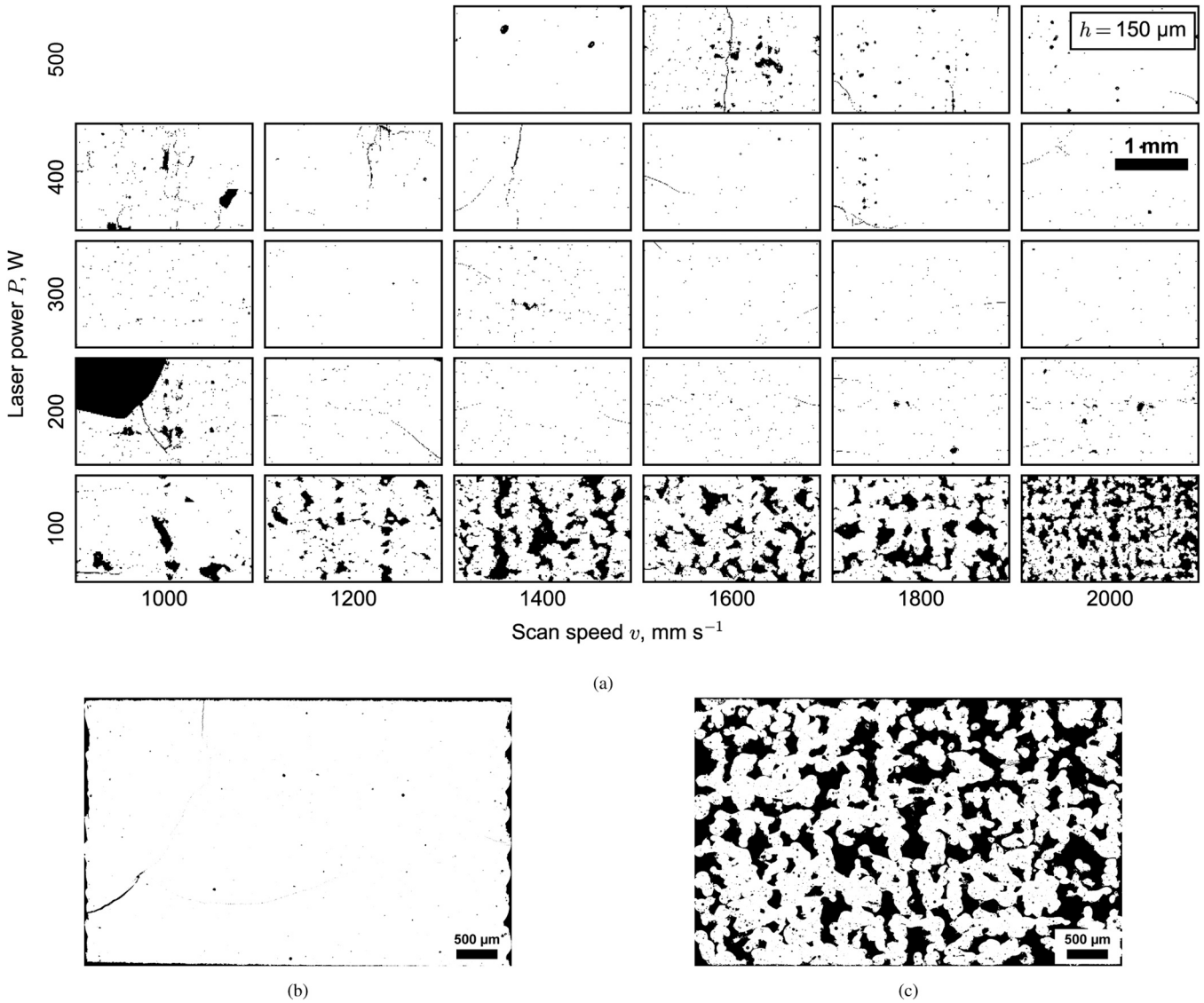

Fig. 4. The optical images of the polished front side of the additively manufactured samples at $h = 150$ μm for (a) the full set, (c) a minimal planar porosity ϕ (~0.2 vol.%) and (c) a maximum ϕ (~37.4 vol.%). The corresponding laser energy densities are 33 J mm^{-3} (300 W, 1200 mm s^{-1}) and 7 J mm^{-3} (100 W, 2000 mm s^{-1}), respectively.

sample (FWHM) of 0.5 × 1.1 mm^2 and exposure time of 60 s–180 s. The sample-to-detector distance was set at 1000 mm and calibrated using Data Analysis WorkbeNch (DAWN) software and a standard LaB_6 sample. Finally, data were integrated and converted into intensity (counts) tables × 2θ using also the DAWN software.

Scanning transmission electron microscopy (STEM) was used to analyze the structural and chemical distribution on the nm scale. A TEM lamellae were prepared with focused-ion beam lift-out from a polished sample using a FEI Nova NanoLab 200 dual-beam SEM (FEI Company, Hillsboro, USA) and a FEI Helios G4 UX (Thermo Fisher Scientific Inc., Waltham, USA). The sample was analyzed using a Thermo Fisher Spectra 300 TEM operating at 300 kV and a FEI Titan G2 80–200, and a FEI Tecnai T20 operating at 200 kV. EDXS was performed in STEM mode using a Thermo Fisher Super-X detector on a Titan G2 80–200. The Thermo Fisher Velox software was used to analyze the EDXS data.

2.3. Thermal analysis

The differential scanning calorimetry (DSC) was performed using the TGA/DSC 3+ thermal analysis system (Mettler-Toledo International Inc., Greifensee, Switzerland). The heating and cooling rates were ~0.167 K s^{-1} from room temperature to 973 K under Ar atmosphere. A second DSC run was used under the same experimental conditions for each sample to accurately plot the baseline [48].

3. Results and discussion

3.1. Process window analysis

Fig. 3a presents the planar porosity ϕ as a function of the input e for different h. While additional cuts on a few representative samples could provide further insight into measurement variability [49,50], the large number of individual samples analyzed (~20–25 per each h) already demonstrates clear trends in porosity, including its reduction that mirrors the behavior observed in L-PBF-processed material, regardless of h. The maximum registered porosity value ϕ changes to lower values of e as h increases. Thus, samples fabricated at $h = 200$ μm show maximum porosity up to ϕ ~46 vol.% at e ~5 J mm^{-3}. This is due to the large distance between the laser tracks, resulting in insufficient melting and the formation of gas voids between the unmelted particles. In the region

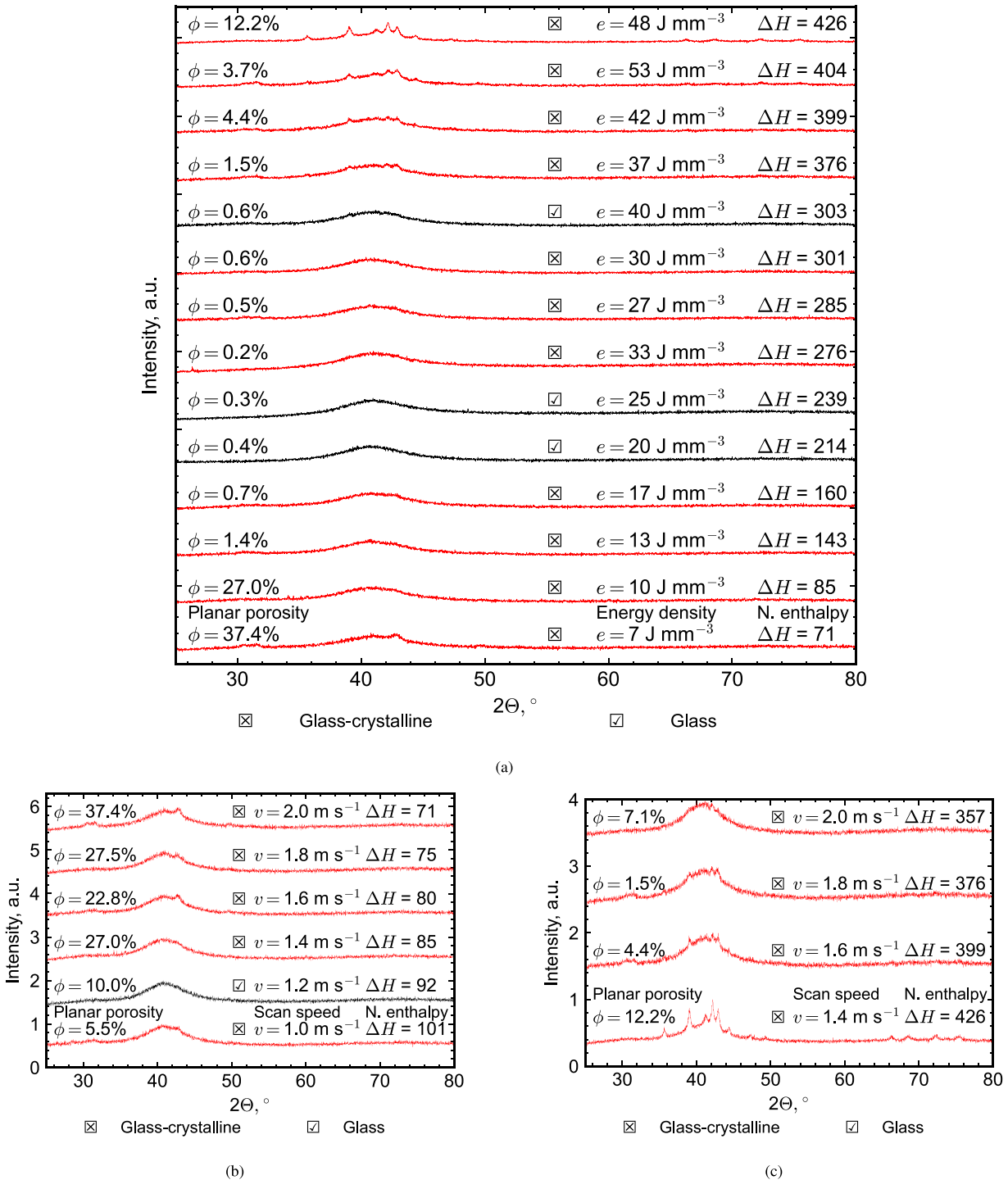

Fig. 5. XRD results (a) of a certain set of samples fabricated at $h = 150$ μm as function of input e ("Energy density") and normalized enthalpy ΔH ("N. enthalpy"), as a function of v at constant P: (b) 100 W and (c) 500 W. The left column presents the corresponding planar porosity ϕ in %. Samples corresponding to glass and glass–crystalline states are marked in black (☑) and red (☒), respectively. (For interpretation of the references to color in the legend of this figure, see the web version of this manuscript.)

$e < \sim$15 J mm^{-3}, at constant e, the maximum porosity is observed at the minimum h. This suggests that for the same values e, the porosity in samples synthesized at the same laser power P is more sensitive to the laser scan speed v than to the hatch spacing h. The increased porosity near $e \sim$42 J mm^{-3} may arise from the superposition of intense Marangoni convection and recoil pressure, leading to the coalescence of gas bubbles trapped within the melt pool [51,52]. Since the planar porosity trends are similar for the considered h, further analyses presented below focus mainly on the sample deposited with $h = 150$ μm. Fig. 3b specifies the interpolation map of planar porosity when P and v vary at constant $h = 150$ μm. This map constrains the process window by suggesting parameters that result in a porosity less than $\phi \sim$5 vol.% (moderate porosity). Note that the red exceptions represent empty data points (complete absence of a sample or absence of a large sample fragment), which are excluded from the interpolation. To view the further plotted mappings for $h = 100$ μm and $h = 200$ μm, see the corresponding

Table 2
The thermophysical properties and other parameters used for the calculations.

Physical property	Symbol	Value	Unit
Density of solid	ρ_s	6.7×10^{-6}[a]	g m^{-3}
Specific heat capacity	c_p	4156×10^{-6}[b]	J g^{-1} K^{-1}
Melting temperature	T_m	1553[c]	K
Latent heat of melting	L_m	2.531[d]	J g^{-1}
Thermal diffusivity	D_s	323×10^{-6}[e]	m^2 s^{-1}
Powder absorbance	α	0.302[f]	–
Half-width of Gaussian beam at surface	r	32×10^{-6}[g]	m

[a] The value is taken from the safety data sheet at $T = 293$ K and $p = 1013$ hPa.
[b] The value is calculated based on [53] in units of J g atom^{-1} K^{-1}, and then converted to J g^{-1} K^{-1} by dividing by the molar mass of the powder $\mu = 6198$ g mol^{-1}. The temperature range is taken between room T_0 and $T_g = 680$ K (Table 4).
[c] The value is taken from the safety data sheet at $p = 1013$ hPa.
[d] The value is calculated using the entropy of melting S_m [53]. $L_m = S_m T_m^{-1} \mu^{-1}$.
[e] The value is calculated using the thermal conductivity κ [54]. $D_s = \kappa \rho_s^{-1} c_p^{-1}$.
[f] The value is taken for pure Cu powder at $\lambda = 1070$ nm [55,56].
[g] The value is taken from the laser acoustic testing.

supplementary Fig. S.1.

Fig. 4a shows the result of the optical microscopy analysis for samples printed at $h = 150$ μm, featuring low and high porosity, Fig. 4b and Fig. 4c, respectively. To view further results of the mappings plotted for $h = 100$ μm and $h = 200$ μm, see the corresponding supplementary Fig. S.2–3. As can be seen in Fig. 4b, the spherical-shaped pores are dominated and induced by trapped gas in a molten pool. The porosity value ϕ is about 0.2 vol.% at the average porosity size of about 100 μm. The sample has distinct cracks near the substrate (bottom part) and around the periphery. This is probably the result of high residual stress. A major crack begins on the left side and propagates within the sample. The observed crack (which stands out in the image) collides with a pore, resulting in directional splitting and subsequent propagation with attenuation. Fig. 4c illustrates the maximum planar porosity (ϕ ~37.4 vol.%) that is expressed by the irregular-shaped pores (low e). Almost all samples fabricated at low e (< ~10 J mm^{-3}) are crack-free or their amount is negligible (~0.02 vol.%). This can be attributed to the significant role of the lack of fusion porosity in cooling conditions. Natural porosity effectively redistributes the internal thermal stresses generated during laser processing. An artificially gyroid porous sample (ϕ in the struts goes zero, while the artificial porosity Φ ~50 %), printed under the same conditions as the bulk sample, exhibited the absence of internal cracks or their volume fraction was negligible. Since the porous 3D printed part undergoes a higher cooling rate (quenching effect), it exhibits a more vitrified state compared to the bulk material, as confirmed by XRD analysis (not shown here). Although these findings demonstrate that pores act as stress-relief zones, preventing crack formation, while nearly bulk samples are significantly more prone to cracking, further investigation through mechanical testing and numerical simulations is needed to fully understand this behavior.

3.2. Microstructural and phase analysis

3.2.1. The crystal formation as function of porosity and cracks

Fig. 5a illustrates the XRD patterns of some samples printed at $h = 150$ μm, obtained using an in-house diffractometer or laboratory XRD. The XRD results obtained for all samples printed with the same $h = 150$ μm are shown in the corresponding supplementary Fig. S.4. The black and red colors indicate the absence or presence of crystal peaks, respectively. As expected, a printed glassy material demonstrates a broad diffraction maximum (characteristic halo) ranging between 30° and 50°. Although the XRD analysis primarily provides information from the surface layer, the amount of crystalline phase is minimal, allowing the sample to be considered nearly glassy. Based on this observation, some 3D printed samples are partially crystalline, while others remain fully glassy. The glassy state of several samples has also been confirmed through synchrotron XRD analysis, which characterized the bulk sample volumes (1 mm in thickness), as discussed in further detail in Section 3.2.2.

In the following, the correlation between the phase composition of the 3D printed samples and the parameters e and ΔH is analyzed. The dimensionless normalized enthalpy ΔH is derived as follows [37]:

$$\Delta H \approx \frac{\alpha P}{\rho_s (c_p (T_m - T_0) + L_m) \sqrt{\pi D_s r^3 v}}, \quad (1)$$

where α is the powder absorbance, ρ_s is the theoretical solid material density, c_p is the specific heat capacity, T_m is the melting temperature of powder, T_0 is the room temperature, L_m is the latent heat of melting, D_s is the thermal diffusivity of powder and r is the half-width of Gaussian beam at surface. Table 2 summarizes the input data used to estimate ΔH.

The nearly glassy state is observed for samples synthesized predominantly in the range 11 J mm^{-3} $\leq e \leq$ 25 J mm^{-3} and 92 $\leq \Delta H \leq$ 239, for e and ΔH, respectively (Fig. 5a and Fig. S.4). The highlighted range of e, applicable to crystal-free samples, partially overlaps with the data provided in the literature [30–32,57]. As shown in [37], the samples printed with the same e exhibited clear differences in phase composition. However, in this work, three samples with the similar e ~33 J mm^{-3} revealed minimal variation in phase composition (Fig. S.4).

To demonstrate the role of high porosity in influencing phase composition, three samples having similar planar porosity ϕ ~26 vol.% have been selected (Fig. S.4). All three are identified as glass–crystalline composites regardless of the values $\Delta H = 75$, 85 and 202. In contrast, samples with similar but lower planar porosity ϕ ~10 vol.% exhibited different phase compositions, resulting in a glass–crystalline state for $\Delta H = 426$ and a predominantly glassy state for $\Delta H = 92$. Although it is challenging to identify an explicit correlation in the nearly random coupling of ΔH and ϕ, it can be observed that values of $\Delta H < 92$ fail to produce higher relaxation and minimal crystallinity [37]. This is probably attributed to both the magnitude of ΔH and the presence of a lack of fusion porosity. This emphasizes that crystallization in these samples is more sensitive to the porosity fraction than to the processing parameter. In contrast, the devitrification of the samples seems weakly correlated with porosity in the keyhole regime. However, further analyses are needed to validate this hypothesis more clearly.

To illustrate the effect of the process parameters such as P and v on the glass or crystal regime, Fig. 5b–c show the generalised results for $P =$ 100 W and $P = 500$ W, respectively. At $P = 500$ W, an increase in v is more favorable to the reduction of crystal formation, while at $P =$ 100 W, samples fabricated at high v show more pronounced crystalline peaks. To explore further dependencies of P and v on crystal formation, see the Supplementary Fig. S.5.

The L-PBF involves thermal cycles over time, which can encourage the overall temperature of the material to rise above the glass transition temperature T_g. As is known, above this temperature, the material will transform into a metastable supercooled liquid, from which further relaxation will occur with the formation of the first crystals. The cooling rate needed to bypass devitrification during MG synthesis depends significantly on the chemical composition of the system and the content of glass former elements such as Zr and Ti [58]. According to [48], the critical cooling rates for Cu-based MG is ~70–250 K s^{-1}, which are significantly lower than the cooling rates obtained in the L-PBF process (~10^6–10^7 K s^{-1}) [59]. This fact emphasizes that continuous devitrification of the material from the liquid to the crystalline phase is highly unlikely due to a high non-equilibrium.

The relationship between crystalline phase formation and porosity at low and high e remains an open question and requires further investigation through numerical simulations (beyond the scope of this manuscript). Although porous samples obtained in the keyhole regime exhibit

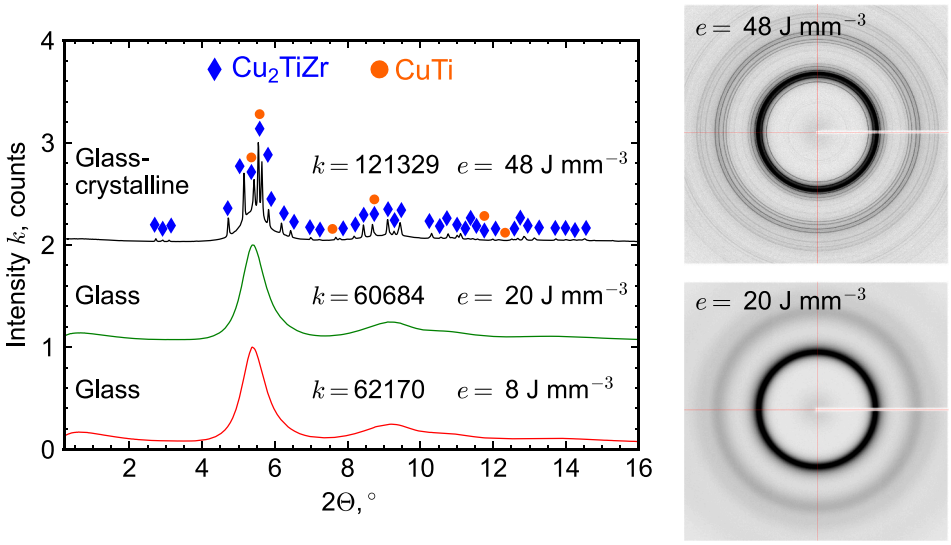

Fig. 6. Synchrotron results obtained for samples printed at low, moderate and high *e*. Sample printed at $e = 48$ J mm^{-3} contains indicated crystalline phases. (For interpretation of the references to color in the legend of this figure, see the web version of this manuscript.)

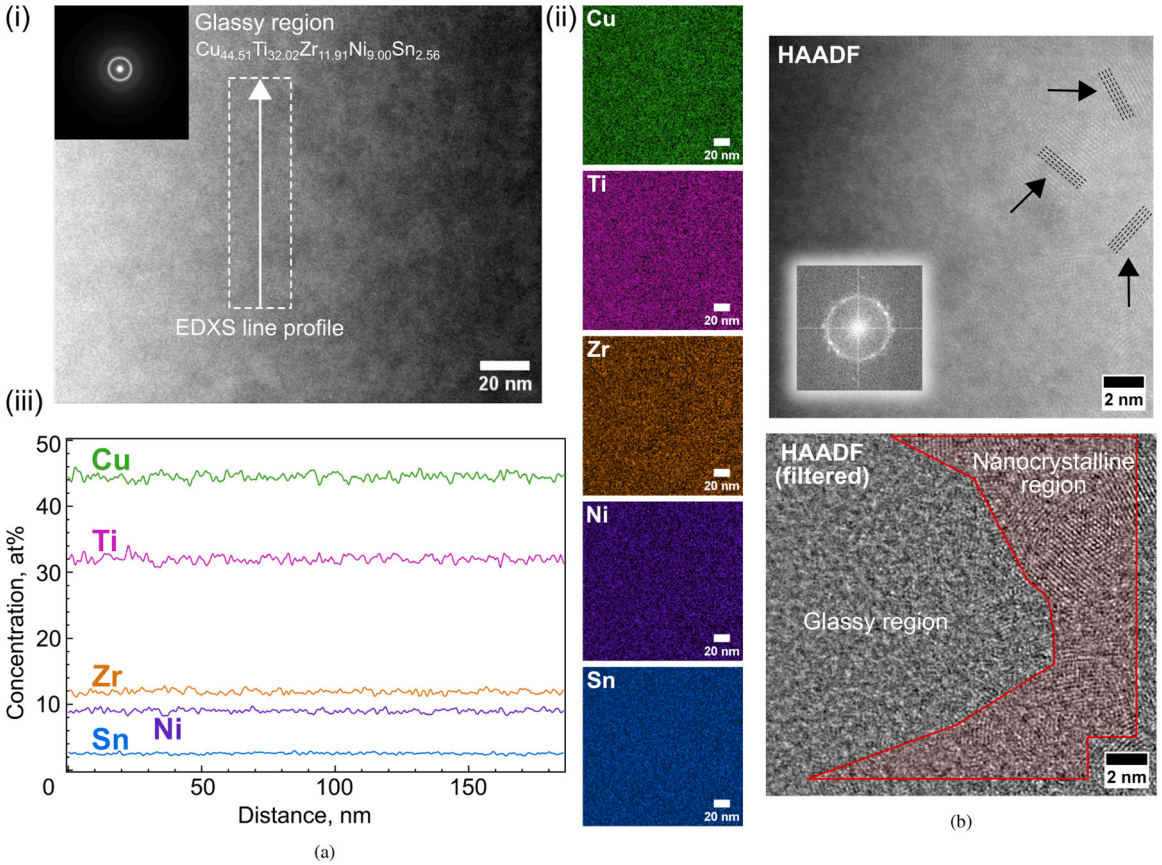

Fig. 7. (a) (i): STEM-HAADF image with the SAED pattern obtained from the glassy region of the sample printed at 20 J mm^{-3}, (ii): the EDXS elemental maps of Cu, Ti, Zr, Ni, and Sn, and (iii): the EDXS line profile taken from (i); (b) The raw (upper) and filtered (lower) STEM-HAADF images at the atomic scale show predominantly a glassy state with nanocrystalline region highlighted in the red area. (For interpretation of the references to color in the legend of this figure, see the web version of this manuscript.)

a weak correlation between porosity and the crystalline phase, the latter can be explained by element segregation induced by Marangoni convection before devitrification within the melt pool. Another point is that the keyhole porosity is smaller in magnitude than the lack of fusion porosity, resulting in a lower cooling rate, which may increase the average temperature of the entire part. This temperature difference becomes significant and can exceed the thermal stability ΔT ($T_{x1} - T_g$, where T_{x1} indicates the first crystallization event) of the supercooled liquid. It will later be shown by DSC that the thermal stability ΔT of the supercooled liquid in the studied material is ~42 K. Despite both the

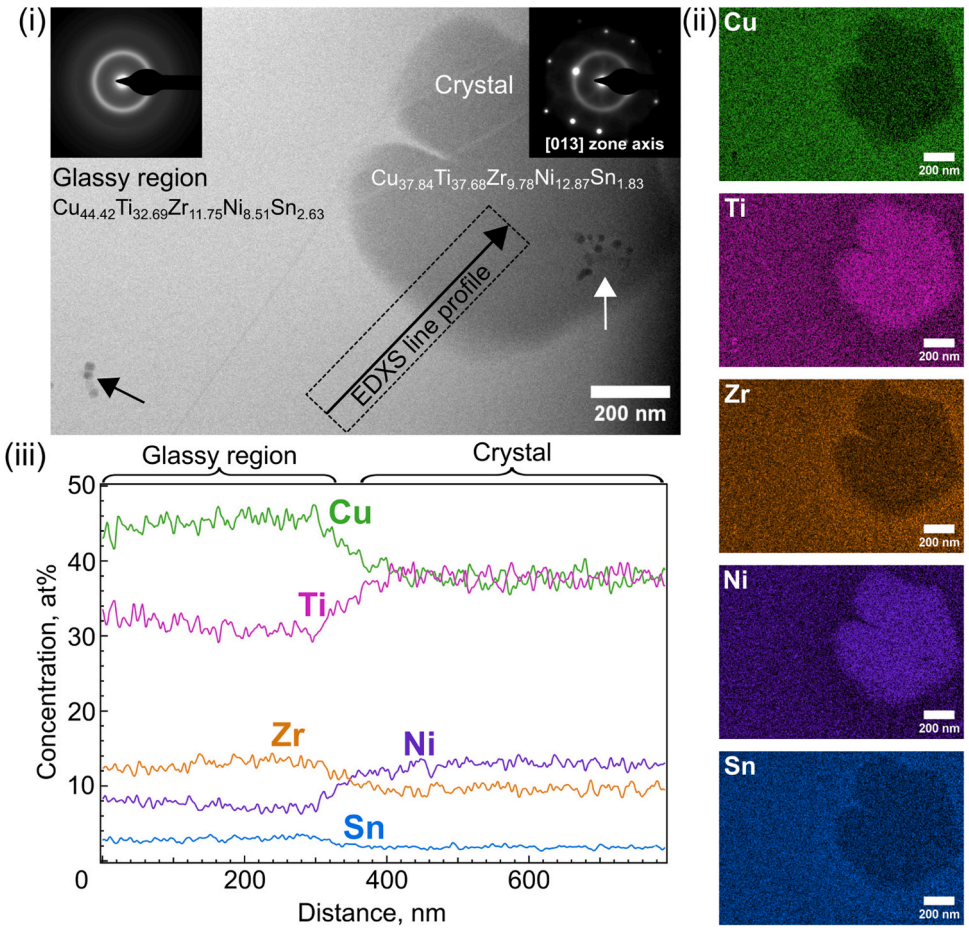

Fig. 8. STEM-HAADF image (i) of the sample printed at 22 J mm^{-3} with insert SAED patterns obtained from the glassy and crystalline regions, (ii) the EDXS elemental maps of Cu, Ti, Zr, Ni, and Sn, and (iii) the line profile taken from (i). (For interpretation of the references to color in the legend of this figure, see the web version of this manuscript.)

natural lack of fusion porosity and the artificial porosity leading to crack-free samples, the smaller magnitude of the lack of fusion porosity may be sufficient to prevent crack formation while still promoting crystallization.

3.2.2. *The spatial distribution of glassy and crystalline phases and their identification*

The identification of nanocrystalline phases and crystals with small volume fractions was conducted using a synchrotron XRD analysis. This method was chosen to investigate the larger recorded volume and ensure accurate phase identification. Three samples with low (8 J mm^{-3}), moderate (20 J mm^{-3}), and high (48 J mm^{-3}) e values were selected (Fig. 6). It is noticeable that samples printed at e = 8 J mm^{-3} and e = 20 J mm^{-3} exhibit two halos, which typically indicates the formation of a glass structure. This suggests that most of the volume is formed by disordered atomic stacking. STEM analysis was performed to further verify the structure and elemental distribution of the sample printed at e = 20 J mm^{-3}. In the high-angle annular dark-field (HAADF) STEM image (Fig. 7a,i), the sample has a glassy structure, as confirmed by the halo feature in the selected area electron diffraction (SAED) pattern. According to the EDXS elemental maps (Fig. 7a,ii), a glassy region has a uniform elemental distribution with a chemical composition of $Cu_{44.51}Ti_{32.02}Zr_{11.91}Ni_{9.00}Sn_{2.56}$. Although the STEM-HAADF image (Fig. 7a,i) shows some color changes, Fig. 7a,iii summarizes the results of the EDXS line profile, which confirms the absence of elemental segregation. The nanocrystalline regions are found in isolated places, as shown in Fig. 7b. The raw (upper) and filtered (lower) STEM-HAADF images demonstrate predominantly glassy structures with partially ordered structures highlighted in the red area at the atomic scale.

To demonstrate the effect of e change on a glassy state stability, STEM analysis was performed on the sample printed at 10 % higher e (22 J mm^{-3}). Similarly to the previous sample, the sample is primarily glass, while several crystalline phases are detected (Fig. 8i). A dark contrast particle with a diameter of 800 nm is a crystalline phase with a face-centered cubic (FCC) structure, according to the SAED pattern. Tiny nanocrystals with a diameter of 20 nm are observed, as indicated with arrows. Fig. 8ii shows the EDXS elemental maps, which illustrate the enrichment of Ti and Ni within the crystalline phase. Fig. 8iii summarizes the results of the EDXS line profile, confirming the variations in the chemical composition between the glass and the crystalline phases. The chemical composition of the glass and the FCC phase was analyzed as $Cu_{44.42}Ti_{32.69}Zr_{11.75}Ni_{8.51}Sn_{2.63}$ and $Cu_{37.84}Ti_{37.68}Zr_{9.78}Ni_{12.87}Sn_{1.83}$, respectively. The glass composition is comparable to that of the sample printed at 20 J mm^{-3}. These results further confirm that a slight change in e can promote and maintain vitrification (inhibit crystallization) or induce devitrification. In the case of devitrification, the nucleation and growth rates of precipitates depend on both temperature and time [60]. Tiny 20 nm nanocrystals precipitate in both the glassy matrix and within the already formed 800 nm crystal. This suggests that the large crystal nucleated and grew largely independently of the tiny nanocrystals and experienced different annealing conditions.

The sample printed at high e = 48 J mm^{-3} has a more pronounced crystalline pattern, although the two halos are visible (Fig. 6). The two predicted phase candidates such as CuTi and Cu_2TiZr have been considered the main possible [61]. According to the SEM micrograph

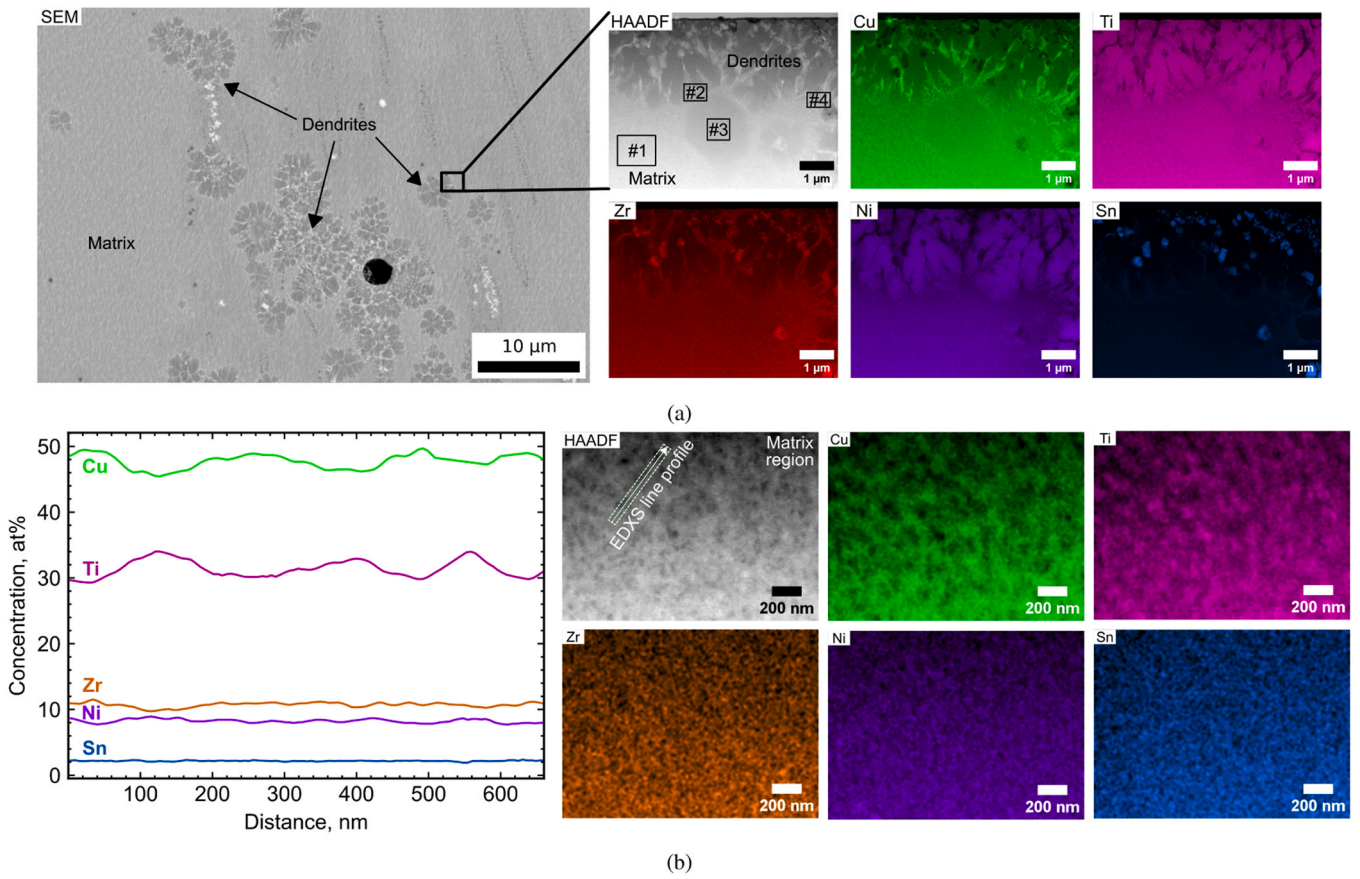

Fig. 9. (a) SEM micrograph providing an overview of the sample printed at 48 J mm^{-3}, accompanied by STEM-HAADF images of a lamella with EDXS analysis results obtained; (b) STEM-HAADF imaging of the "Matrix" region taken from (a), including the results of the EDXS analysis. (For interpretation of the references to color in the legend of this figure, see the web version of this manuscript.)

Table 3
Summary of the identified element distribution taken from glass–crystalline region of the lamella.

Area Element, at. %	#1	#2	#3	#4	Feedstock
Cu	48.88 ± 3.71	50.99 ± 3.71	48.35 ± 3.70	54.81 ± 3.69	45.38
Ti	31.12 ± 2.31	29.76 ± 2.30	32.29 ± 2.37	26.67 ± 2.20	34.30
Zr	10.50 ± 1.42	10.44 ± 1.43	10.36 ± 1.40	11.06 ± 1.53	11.12
Ni	8.04 ± 1.23	7.51 ± 1.16	7.84 ± 1.20	6.31 ± 1.01	8.07
Sn	1.45 ± 0.19	1.31 ± 0.17	1.17 ± 0.15	1.15 ± 0.15	1.14

(Fig. 9a), the distribution of the crystal phases and their size are variable and appear to be random within space [43]. The observed microstructure can hardly be characterized at this scale as featureless because of the crystal pattern. To verify the two main assumed phases, a thorough STEM-EDXS study was performed to obtain stoichiometric ratios on a large scale. The matching procedure was performed using NanoMEGAS software (EMSIS GmbH, Münster, Germany). The extracted lamella (Fig. 9a) consists of a glass–nanocrystalline matrix with large crystalline inclusions, as confirmed by SAED (not shown here). This is due to the contribution of a high value of *e*, which leads to a reduction in the free energy of the system due to the local atomic order [4,7,48]. On a larger scale, a visible transition is observed from a more homogeneous structure to a branched structure. Despite the adequate fitting of Cu_2TiZr shown in Fig. 6, this phase is absent in the extracted lamella, while only the CuTi phase is correctly fitted and detected by STEM analysis. This can be explained by the accepted assumption of a solid solution and the spatial absence of a specific phase in the lamella. The color elemental mappings assessed by STEM-EDXS, as shown in Fig. 9a, help to evaluate the distribution of elements within the glass–crystalline region of the lamella. Although Cu is the dominant component of the alloy and serves as a solvent for the other elements, bright branch-shaped Cu regions are observed in the Ti matrix. Sn particles appear to be dispersed in the Ti matrix as can be seen highlighted in blue. Zr is locally correlated with Cu and Sn. The HAADF image, as shown in Fig. 9a, includes areas marked as *#i*, whose compositions have been analyzed. Table 3 summarizes the results of the microanalysis by area performed using the STEM-EDXS. Although the atomic content of Cu remains within the error margin for observed #1, #3, and the feedstock, the absolute value of Cu must be taken carefully, since the lamella was mounted on a Cu TEM grid, which could lead to an increase in the measured Cu signal. Note that the precision of the chemical composition of the two previously analyzed STEM lamellae in 20 J mm^{-3} and 22 J mm^{-3} differs from that of the lamella analyzed in 48 J mm^{-3} due to the use of different STEM systems. The Cu–Ti ratio of region #4 is slightly higher compared to the #1, #2, #3 and parent alloy. According to the stoichiometric relations, CuTi and Cu_2Ti phases can be formed, as shown above. This can be explained by local segregation at the beginning of the melting, driven by their negative mixing enthalpy [62].

Fig. 9b presents the chemical analysis results using STEM-EDXS of the "Matrix" region shown in Fig. 9a. Pronounced chemical segregation can be observed at a higher resolution, which differs from the glassy region depicted in Fig. 7a,i. The chemical composition of the entire area (Fig. 9b) is similar to #1 (Cu = 48.96 ± 3.71, Ti = 31.01 ± 2.31, Zr =

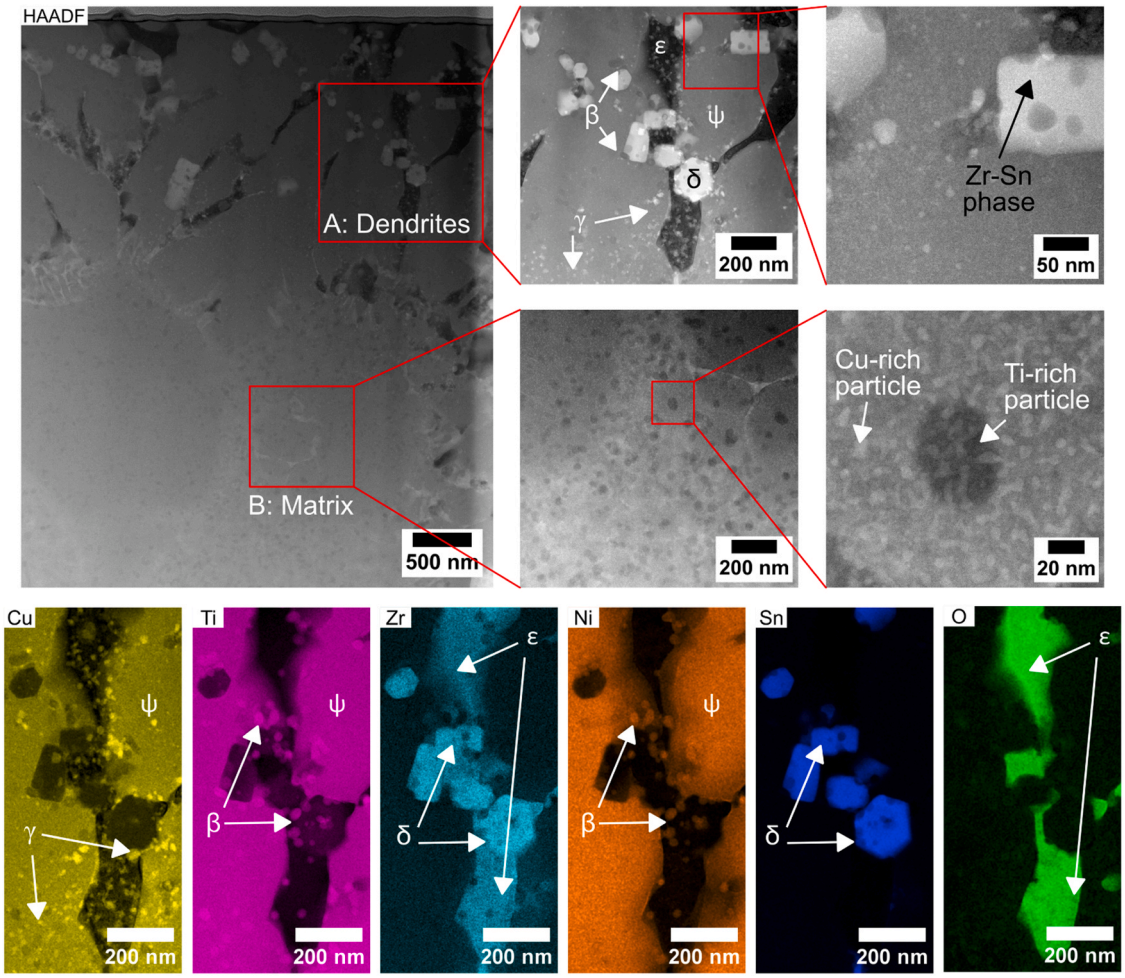

Fig. 10. STEM-HAADF high-resolution images of the matrix and dendritic region in the lamella taken from (Fig. 9a). According to the EDXS analysis, the dendritic region consists of at least five phases such as (ψ) gray Cu–Ti–Ni-rich matrix, (β) Ti–Ni-rich nanoparticles, (γ) Cu-rich nanoparticles, (δ) large bright Zr–Sn-rich crystallites, and (ε) a dark phase of Zr oxide. (For interpretation of the references to color in the legend of this figure, see the web version of this manuscript.)

Table 4
Summary of the identified element distribution taken from the "Dendrites" region of the lamella (Fig. 10).

Element, at.% Phase	Cu	Ti	Zr	Ni	Sn	O
ψ	39.13	33.23	5.91	11.00	0.27	10.46
β	37.99	34.74	6.06	10.12	0.33	10.75
γ	43.15	30.67	6.05	9.05	0.29	10.79
δ	24.44	15.90	24.71	1.05	21.17	12.73
ε	19.51	6.02	17.05	0.95	0.10	56.36

10.60 ± 1.43, Ni = 7.99 ± 1.22, Sn = 1.44 ± 0.19, all in at.%). This segregation can be explained by increased atomic relaxation to form close packing due to the wide distribution of atomic radii and the corresponding mixing enthalpies [63]. It can be seen qualitatively, the characteristic nanocrystal size is higher for 3D printed samples (~100 nm) compared to atomized powder (~5–15 nm) or melt spinning ribbon (~20 nm) [48,64]. This highlights the influence of cumulative thermal effects during L-PBF, which are absent in melt spinning.

To obtain more detailed information on the crystalline phases, STEM-EDXS analysis (Fig. 10) was conducted at high-resolution on a lamella extracted from a sample printed at 48 J mm^{-3} (Fig. 9a). The small region appears to be relatively complex with respect to the number of phases. The matrix region (B) close to the dendritic region (A) was examined to observe the microstructural changes affected by proximity to the crystals. According to the Fourier transform (not shown here), the material shows an inner structure. The HAADF image shows bright Cu-rich particles with a size of around 10 nm, as well as dark Ti-rich structures with a size of approximately 50 nm. Chemical analysis shows that the EDXS results for the high-resolution dendritic region (A) are consistent with those obtained from EDXS at low resolution (Fig. 9a). At least five different phases are identified as (ψ) a gray Cu–Ti–Ni-rich matrix, (β) Ti–Ni-rich nanoparticles, (γ) Cu-rich nanoparticles, (δ) large bright crystallites rich in Zr–Sn, and (ε) a dark phase of Zr oxide (with O_2 at approximately 56 at.%), which is polycrystalline (Table 4). Despite the strong oxidation, EDXS quantification of the light element oxygen is prone to errors, so oxidation of the material in general cannot be neglected. The phases γ, ψ, and β show a similar composition of Cu–Ti–Ni. Phase γ contains additional Cu particles, while phase β contains additional Ti particles. Cu is not necessarily present in the phases ε and δ, as it can originate from the grid, small particles, or the projection matrix.

The observed multiphase nanocrystal formation can be explained as follows. Laser processing at high values of e results in an extended HAZ, where the average temperature remains close to or above the glass transition temperature of the alloy [43]. This promotes atomic rearrangement, leading to subsequent crystal formation [7,65]. As shown in [66], the varying annealing conditions affect phase formation and subsequent decomposition into additional phases. Since both the nucleation and growth rates of precipitates are temperature and time dependent [60], the magnitude of laser processing has a significant impact. As

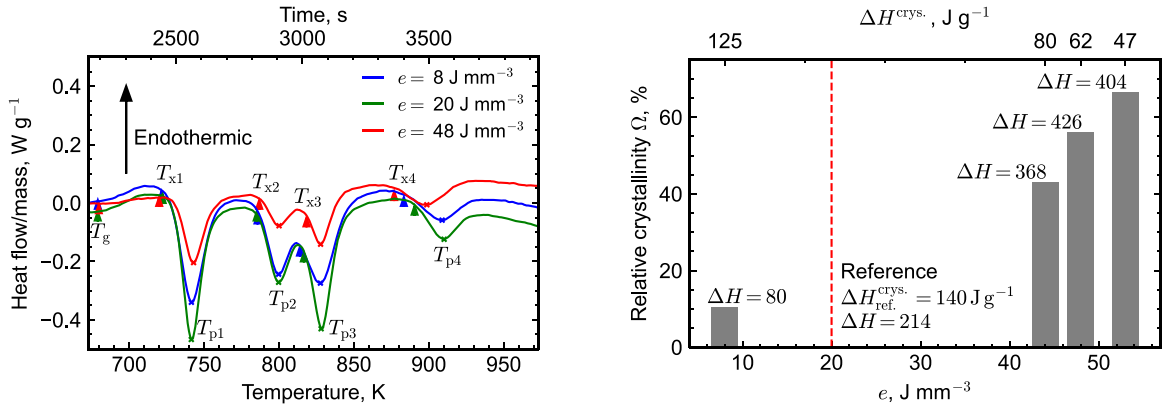

Fig. 11. (a) DSC results of samples printed at different e values. (b) The crystalline fraction Ω as a function of e = 8 J mm^{-3}, 20 J mm^{-3}, 44 J mm^{-3}, 48 J mm^{-3} and 53 J mm^{-3}. (For interpretation of the references to color in the legend of this figure, see the web version of this manuscript.)

Table 5
Summary of DSC results of samples printed at different e. The thermal stability is $\Delta T = T_{x1} - T_g$.

e, J mm^{-3}	$\lvert\Delta H^{crys.}\rvert$, J g^{-1}					T_g, K	T_{x1}, K	ΔT, K
	1st	2nd	3rd	4th	∑			
8	41.3	18.3	50.1	15.5	125.2	679.1	721.6	42.5
20	44.0	20.6	59.4	15.9	139.9	679.0	722.4	43.3
48	21.9	9.2	18.0	12.4	61.5	679.7	720.0	40.3

Temperature, K						
T_{x2}	T_{x3}	T_{x4}	T_{p1}	T_{p2}	T_{p3}	T_{p4}
785.7	814.0	883.3	741.5	799.7	827.6	908.9
785.1	816.6	890.5	741.5	799.7	828.1	910.2
786.8	818.4	876.9	743.0	800.0	827.8	898.7

mentioned in Section 3.2.1, elemental segregation is enhanced in the keyhole regime. Local variations in solute partitioning (solute trapping) [67] can reduce the energy barrier for nucleation, thus increasing the probability of multiphase nanocrystal formation [68].

3.3. Thermal analysis

DSC analysis was performed for three samples obtained at different e (8 J mm^{-3}, 20 J mm^{-3} and 48 J mm^{-3}). Fig. 11 illustrates the resulting DSC traces. All samples exhibit a barely visible endothermic peak typical of MG at T_g, indicating the transition of glass to the supercooled liquid with the following ongoing crystallization events T_{x1} (both temperatures are marked by arrows in Fig. 11). Table 5 provides other important temperatures such as T_{xi}, T_{pi} extracted from the measured DSC curves. The increase in the magnitude of thermal stability ΔT indicates the high resistance to nucleation due to the great atomic rearrangement in the multi-component system [64]. Table 5 shows that ΔT decreases with increasing e, most likely resulting in a transient devitrification of the supercooled liquid [64]. Note that the last exothermic events in Fig. 11 show minimal changes (crystallization enthalpy $\Delta H^{crys.}_{4th}$) with respect to e. The temperature peaks of devitrification/crystallization T_{pi} are similar for the first three peaks, while T_{p4} are not. There is a tendency for samples with a large volume of crystals (e = 48 J mm^{-3}) to move T_{p4} to the low-temperature region. The resulting sums of $\Delta H^{crys.}_{\Sigma} = \sum \Delta H^{crys.}_{i}$ for specific samples are included in Table 5. Qualitatively, the formation of crystalline phases is inversely proportional to $\Delta H^{crys.}_{\Sigma}$, indicating that the higher $\Delta H^{crys.}_{\Sigma}$, the less material undergoes crystallization. The four exothermic peaks are associated with the formation of crystalline phases within the glassy matrix. A sharp first peak may indicate the presence of a particular crystalline phase, while a broader peak may indicate the presence of multiple crystalline phases. Moreover, the 2nd and 3rd peaks most likely indicate the possible formation of a transition phase, which subsequently decomposes into thermodynamically stable phases [64,69,70]. The reduced glass transition temperature T_{rg} is ~0.44, which is lower than 0.5 and indicates low GFA and poor nucleation suppression [7]. Although the observed thermal stability is lower compared to the $Cu_{47}Ti_{34}Zr_{11}Ni_8$ at.% alloy without Sn_2 at.%, the addition of Sn to the alloy should increase resistance to nucleation by increasing the packing density of atoms [48,63,64]. This discrepancy can be attributed to the contribution of repeated thermal cycles and the way heat is released through the material. Thus, under these conditions, it can be assumed that atoms are more prone to spontaneous rearrangements from the supercooled liquid into metastable phases, which by their nature are obliged to undergo further devitrification.

The relative crystalline fraction Ω is calculated as follows: $\Omega = (\Delta H^{crys.}_{ref.} - \Delta H^{crys.}_{i})/\Delta H^{crys.}_{ref.}$, where $\Delta H^{crys.}_{ref.}$ is the crystallization enthalpy of the glass sample, determined by synchrotron XRD analysis (e = 20 J mm^{-3}, ΔH = 214). Fig. 11b illustrates the increase in Ω with increasing e and ΔH, which is in agreement with the literature [33,37,71]. In this work, the crystallization enthalpy of the laser-processed sample, instead of the original powder, is used as a reference. The DSC analysis reveals $\Delta H^{crys.}_{\Sigma}$ of 96.8 ± 4.0 J g^{-1} for the powder and 139.9 J g^{-1} for the bulk printed sample (the highest $\Delta H^{crys.}_{\Sigma}$ value, see Table 5). This difference is attributed to the distinct thermal histories of the powder and the printed part. Specifically, the cooling rates achievable in gas atomization and laser powder bed fusion are 10^2–10^5 K s^{-1} [72] and 10^6–10^7 K s^{-1} [18], respectively. Therefore, although the original powder is initially in a glassy state, its use in estimating the relative crystalline fraction may still introduce inaccuracies. For this reason, in the present manuscript, the highest $\Delta H^{crys.}_{\Sigma}$ obtained in the bulk printed sample was used as a reference $\Delta H^{crys.}_{ref.}$.

4. Conclusion

This study reports on systematic analysis of the laser processing of a $Cu_{45}Ti_{34}Zr_{11}Ni_8Sn_2$ (at.%) glass-forming alloy. Despite its low reduced glass transition temperature T_{rg} ~0.44, the glassy state of the current material can be stabilized within the optimized laser process window. The specific insights of this study are detailed as follows:

- The stabilization of the nearly glassy state of the metallic glass is achieved within a laser energy density 11 J mm^{-3} ≤ e ≤ 25 J mm^{-3} and normalized enthalpy 92 ≤ ΔH ≤ 239 that correlates with moderate porosity values of the obtained samples. The devitrification of

the samples is weakly correlated with porosity in the keyhole regime, whereas it shows a strong correlation in the lack of fusion regime.

- The sample manufactured using the laser energy e outside the 11 J mm^{-3} to 25 J mm^{-3} range possess complex phase composition. For example, the sample obtained at 48 J mm^{-3} is thoroughly analyzed and revealed the presence of at least five different nanocrystalline phases.
- Relative crystallinity Ω is inversely proportional to crystallization enthalpy $\Delta H^{\text{crys.}}$. The thermal stability ΔT of the metallic glass decreases from ~43.3 K to ~40.3 K as e increases from 20 J mm^{-3} to 48 J mm^{-3}, which is explained by the increase in relaxation from the supercooled liquid state to the devitrification state.
- The processing cracks have an inverse correlation with the formation of pores [73,74]. Samples processed in the lack of fusion regime (irregular porosity ϕ ~37.4 vol.%) have fewer or lack of cracks, whereas more pronounced cracks are observed in samples processed in moderate (ϕ ~0.2 vol.%) laser energy and keyhole regimes.

The obtained results illustrate complexity of additive manufacturing of bulk metallic glasses by laser powder bed fusion because of the specific thermal history, namely repeated laser heating of consequent material layers and possible in-process material devitrification. Therefore, the precise in-situ control of thermal history upon laser processing of glassy materials is required to manufacture bulk metallic glass parts for engineering applications.

CRediT authorship contribution statement

Aleksandr M. Filimonov: Writing – review & editing, Writing – original draft, Methodology, Investigation, Data curation. **K.M. Saiful Alam:** Writing – review & editing, Investigation. **Askar R. Kvaratskheliya:** Writing – review & editing, Investigation, Data curation. **Tim Grieb:** Writing – review & editing, Investigation, Data curation. **Binkal Kumar Sharma:** Writing – review & editing, Data curation. **Bruno Bianchini:** Writing – review & editing, Investigation, Data curation. **Rafael Formenton Macedo dos Santos:** Writing – review & editing, Investigation. **Leonardo Fernandes Gomes:** Writing – review & editing, Investigation. **Andreas Rosenauer:** Writing – review & editing. **Piter Gargarella:** Writing – review & editing, Investigation, Data curation. **Nattamon Suwannaharn:** Writing – review & editing, Investigation, Data curation. **Taisuke T. Sasaki:** Writing – review & editing, Investigation, Data curation. **Lutz Mädler:** Writing – review & editing, Supervision, Conceptualization. **Ilya V. Okulov:** Writing – review & editing, Writing – original draft, Supervision, Methodology, Data curation, Conceptualization.

Declaration of Competing Interest

The authors declare that they have no known competing financial interests or personal relationships that could have appeared to influence the work reported in this paper.

Data Availability

Data will be made available on request.

Acknowledgments

The authors gratefully acknowledge funding from the German Federal Ministry for Education and Research under LikeABone project 13XP5151, DAAD-CAPES cooperation project between Brazil and Germany (project ID: 57598551). Andreas Rosenauer acknowledges the German Research Foundation under the INST 144/462–1 FUGG for the Spectra. Besides, the authors acknowledge DESY (Hamburg, Germany), a member of the Helmholtz Association HGF, for the provision of experimental facilities. Parts of this research were carried out at PETRA III, and we thank Alba San Jose Mendez for assistance in using beamline P02.1. Beamtime was allocated for proposal I-2022099. Taisuke T. Sasaki acknowledges the JSPS KAKENHI Grant-in-Aid for Transformative Research Areas (A) "Creation of Materials by Super Thermal Field: Neo-3D printing by Manipulating Atomic Arrangement through Giant Potential Gradient" (Grant Numbers 24H01008) and CREST Nanomechanics: Elucidation of macroscale mechanical properties based on understanding nanoscale dynamics for innovative mechanical materials (Grant Number: JPMJCR2194) from the Japan Science and Technology Agency (JST).

Appendix A. Supporting information

Supplementary data associated with this article can be found in the online version at doi:10.1016/j.jallcom.2025.180339.

References

[1] W.L. Johnson, Bulk metallic glasses — a new engineering material, Curr. Opin. Solid State Mater. Sci. 1 (3) (1996) 383–386, https://doi.org/10.1016/S1359-0286(96)80029-5.
[2] J. Schroers, Processing of bulk metallic glass, Adv. Mater. 22 (14) (2010) 1566–1597, https://doi.org/10.1002/adma.200902776.
[3] A. Inoue, A. Takeuchi, Recent development and application products of bulk glassy alloys, Acta Mater. 59 (6) (2011) 2243–2267, https://doi.org/10.1016/j.actamat.2010.11.027.
[4] C. Suryanarayana, Mechanical behavior of emerging materials, Mater. Today 15 (11) (2012) 486–498, https://doi.org/10.1016/S1369-7021(12)70218-3.
[5] J.J. Kruzic, Bulk metallic glasses as structural materials: a review, Adv. Eng. Mater. 18 (8) (2016) 1308–1331, https://doi.org/10.1002/adem.201600066.
[6] S. Sohrabi, J. Fu, L. Li, Y. Zhang, X. Li, F. Sun, J. Ma, W.H. Wang, Manufacturing of metallic glass components: processes, structures and properties, Prog. Mater. Sci. 144 (2024) 101283, https://doi.org/10.1016/j.pmatsci.2024.101283.
[7] F. Spaepen, Identification of the metallic glass state, Mater. Res. Soc. Symp. Proc. 57 (1987) 162–184, https://doi.org/10.1557/proc-57-161.
[8] E.D. Zanotto, J.C. Mauro, The glassy state of matter: its definition and ultimate fate, J. Non-Cryst. Solids 471 (April) (2017) 490–495, https://doi.org/10.1016/j.jnoncrysol.2017.05.019.
[9] P.K. Gupta, Non-crystalline solids: glasses and amorphous solids, J. Non-Cryst. Solid 195 (1996) 158–164.
[10] X.H. Lin, W.L. Johnson, Formation of Ti-Zr-Cu-Ni bulk metallic glasses, J. Appl. Phys. 78 (11) (1995) 6514–6519, https://doi.org/10.1063/1.360537.
[11] Q. Li, S.S. Liu, X.H. Wang, T. Yang, C. Dong, J.T. Hu, Y.Q. Jiang, Mechanical and corrosion properties of Ti-Ni-Cu-Zr metallic glass matrix composites, J. Alloy. Compd. 727 (2017) 1344–1350, https://doi.org/10.1016/j.jallcom.2017.08.120.
[12] Á. Révész, A. Horváth, G. Ribárik, E. Schafler, D.J. Browne, Z. Kovács, Crystallization of Cu60Zr20Ti20 bulk metallic glass by high pressure torsion, Rev. Adv. Mater. Sci. 58 (1) (2019) 304–312, https://doi.org/10.1515/rams-2019-0037.
[13] N. Li, W. Chen, L. Liu, Thermoplastic micro-forming of bulk metallic glasses: a review, JOM 68 (4) (2016) 1246–1261, https://doi.org/10.1007/s11837-016-1844-y.
[14] B. Sarac, J. Eckert, Thermoplasticity of metallic glasses: processing and applications, Prog. Mater. Sci. 127 (2022) 100941, https://doi.org/10.1016/j.pmatsci.2022.100941.
[15] T. Wada, D.V. Louzguine-Luzgin, A. Inoue, Preparation of Zr-based metallic glass nanowires and nanoparticles by selective etching, Scr. Mater. 57 (10) (2007) 901–904, https://doi.org/10.1016/j.scriptamat.2007.07.032.
[16] Y. Zeng, C. Qin, N. Nishiyama, A. Inoue, New nickel-based bulk metallic glasses with extremely high nickel content, J. Alloy. Compd. 489 (1) (2010) 80–83, https://doi.org/10.1016/j.jallcom.2009.09.016.
[17] P. Gargarella, S. Pauly, M. Samadi Khoshkhoo, U. Kühn, J. Eckert, Phase formation and mechanical properties of Ti-Cu-Ni-Zr bulk metallic glass composites, Acta Mater. 65 (2014) 259–269, https://doi.org/10.1016/j.actamat.2013.10.068.
[18] I. Gibson, D. Rosen, B. Stucker. Additive manufacturing technologies: 3D printing, rapid prototyping, and direct digital manufacturing, second edition, 2015, https://doi.org/10.1007/978-1-4939-2113-3.
[19] P. Bordeenithikasem, Y. Shen, H.L. Tsai, D.C. Hofmann, Enhanced mechanical properties of additively manufactured bulk metallic glasses produced through laser foil printing from continuous sheetmetal feedstock, Addit. Manuf. 19 (2018) 95–103, https://doi.org/10.1016/j.addma.2017.11.010.
[20] P. Bordeenithikasem, M. Stolpe, A. Elsen, D.C. Hofmann, Glass forming ability, flexural strength, and wear properties of additively manufactured Zr-based bulk metallic glasses produced through laser powder bed fusion, Addit. Manuf. 21 (2018) 312–317, https://doi.org/10.1016/j.addma.2018.03.023.
[21] L. Deng, S. Wang, P. Wang, U. Kühn, S. Pauly, Selective laser melting of a Ti-based bulk metallic glass, Mater. Lett. 212 (2018) 346–349, https://doi.org/10.1016/j.matlet.2017.10.130.
[22] N. Sohrabi, J. Jhabvala, R.E. Logé, Additive manufacturing of bulk metallic glasses—process, challenges and properties: A review, Metals 11 (8) (2021), https://doi.org/10.3390/met11081279.

[23] P. Zhang, J. Tan, Y. Tian, H. Yan, Z. Yu, Research progress on selective laser melting (SLM) of bulk metallic glasses (BMGs): a review, Int. J. Adv. Manuf. Technol. 118 (7-8) (2022) 2017–2057, https://doi.org/10.1007/s00170-021-07990-8.
[24] C. Zhang, D. Ouyang, S. Pauly, L. Liu, 3D printing of bulk metallic glasses, Mater. Sci. Eng. R: Rep. 145 (2021), https://doi.org/10.1016/j.mser.2021.100625.
[25] S. Hadibeik, H. Ghasemi-Tabasi, A. Burn, S. Lani, F. Spieckermann, J. Eckert, Controlling the glassy state toward structural and mechanical enhancement: additive manufacturing of bulk metallic glass using advanced laser beam shaping technology, Adv. Funct. Mater. 34 (12) (2024) 2311118, https://doi.org/10.1002/adfm.202311118.
[26] F. Spaepen, D. Turnbull, Metallic Glasses, Annu. Rev. Phys. Chem. 35 (1) (1984) 241–263, https://doi.org/10.1146/annurev.pc.35.100184.001325.
[27] H. Sun, K.M. Flores, Laser deposition of a Cu-based metallic glass powder on a Zr-based glass substrate, J. Mater. Res. 23 (10) (2008) 2692–2703, https://doi.org/10.1557/jmr.2008.0329.
[28] S. Pauly, L. Löber, R. Petters, M. Stoica, S. Scudino, U. Kühn, J. Eckert, Processing metallic glasses by selective laser melting, Mater. Today 16 (1-2) (2013) 37–41, https://doi.org/10.1016/j.mattod.2013.01.018.
[29] X.P. Li, C.W. Kang, H. Huang, T.B. Sercombe, The role of a low-energy-density re-scan in fabricating crack-free Al85Ni5Y6Co2Fe2 bulk metallic glass composites via selective laser melting, Mater. Des. 63 (2014) 407–411, https://doi.org/10.1016/j.matdes.2014.06.022.
[30] X. Lu, M. Nursulton, Y. Du, W. Liao, Structural and mechanical characteristics of Cu50Zr43Al7 bulk metallic glass fabricated by selective laser melting, Materials 12 (5) (2019), https://doi.org/10.3390/ma12050775.
[31] E. Soares Barreto, V. Uhlenwinkel, M. Frey, I. Gallino, R. Busch, A. Lüttge, Influence of Processing Route on the Surface Reactivity of Cu47Ti33Zr11Ni6Sn2Si1 Metallic Glass, Metals 11 (8) (2021), https://doi.org/10.3390/met11081173.
[32] M. Frey, J. Wegner, E.S. Barreto, L. Ruschel, N. Neuber, B. Adam, S.S. Riegler, H.-R. Jiang, G. Witt, N. Ellendt, V. Uhlenwinkel, S. Kleszczynski, R. Busch, Laser powder bed fusion of Cu-Ti-Zr-Ni bulk metallic glasses in the Vit101 alloy system, Addit. Manuf. 66 (2023) 103467, https://doi.org/10.1016/j.addma.2023.103467.
[33] N. Sohrabi, T. Ivas, J. Jhabvala, J.E.K. Schawe, J.F. Löffler, H. Ghasemi-Tabasi, R. E. Logé, Quantitative prediction of crystallization in laser powder bed fusion of a Zr-based bulk metallic glass with high oxygen content, Mater. Des. 239 (2024) 112744, https://doi.org/10.1016/j.matdes.2024.112744.
[34] L.-Y. Chen, S.-X. Liang, Y. Liu, L.-C. Zhang, Additive manufacturing of metallic lattice structures: unconstrained design, accurate fabrication, fascinated performances, and challenges, Mater. Sci. Eng.: R: Rep. 146 (2021) 100648, https://doi.org/10.1016/j.mser.2021.100648.
[35] A. Paraschiv, G. Matache, N. Constantin, M. Vladut, Investigation of scanning strategies and laser remelting effects on top surface deformation of additively manufactured IN 625, Materials 15 (9) (2022), https://doi.org/10.3390/ma15093198.
[36] P. Promoppatum, S.C. Yao, P.C. Pistorius, A.D. Rollett, A comprehensive comparison of the Analytical and numerical prediction of the thermal history and solidification microstructure of Inconel 718 products made by laser powder-bed fusion, Engineering 3 (5) (2017) 685–694, https://doi.org/10.1016/J.ENG.2017.05.023.
[37] S. Hadibeik, E. Gingl, L. Schretter, B. Bochtler, J. Li, C. Gammer, A. Hohenwarter, F. Spieckermann, J. Eckert, Semi-analytical and experimental heat input study of additively manufactured Zr-based bulk metallic glass: insights into nano- and global-scale relaxation and crystallization, Addit. Manuf. 89 (July) (2024) 104295, https://doi.org/10.1016/j.addma.2024.104295.
[38] D.B. Hann, J. Iammi, J. Folkes, A simple methodology for predicting laser-weld properties from material and laser parameters, J. Phys. D: Appl. Phys. 44 (44) (2011), https://doi.org/10.1088/0022-3727/44/44/445401.
[39] A.M. Rubenchik, W.E. King, S.S. Wu, Scaling laws for the additive manufacturing, J. Mater. Process. Technol. 257 (2018) 234–243, https://doi.org/10.1016/j.jmatprotec.2018.02.034.
[40] M.C. Sow, T. De Terris, O. Castelnau, Z. Hamouche, F. Coste, R. Fabbro, P. Peyre, Influence of beam diameter on Laser Powder Bed Fusion (L-PBF) process, Addit. Manuf. 36 (2020) 101532, https://doi.org/10.1016/j.addma.2020.101532.
[41] S. Bergmueller, L. Gerhold, L. Fuchs, L. Kaserer, G. Leichtfried, Systematic approach to process parameter optimization for laser powder bed fusion of low-alloy steel based on melting modes, Int. J. Adv. Manuf. Technol. 126 (9) (2023) 4385–4398, https://doi.org/10.1007/s00170-023-11377-2.
[42] K. Kosiba, D.Y. Kononenko, D. Chernyavsky, L. Deng, J. Bednarcik, J. Han, J. van den Brink, H.J. Kim, S. Scudino, Maximizing vitrification and density of a Zr-based glass-forming alloy processed by laser powder bed fusion, J. Alloy. Compd. 940 (2023) 168946, https://doi.org/10.1016/j.jallcom.2023.168946.
[43] Ł. Żrodowski, R. Wróblewski, M. Leonowicz, B. Morończyk, T. Choma, J. Ciftci, W. Święszkowski, A. Dobkowska, E. Ura-Bińczyk, P. Błyskun, J. Jaroszewicz, A. Krawczyńska, K. Kulikowski, B. Wysocki, T. Cetner, G. Moneta, X. Li, L. Yuan, A. Małachowska, R. Chulist, C. Żrodowski, How to control the crystallization of metallic glasses during laser powder bed fusion? Towards part-specific 3D printing of in situ composites, Addit. Manuf. 76 (September) (2023), https://doi.org/10.1016/j.addma.2023.103775.
[44] X. Ye, Y.C. Shin, Synthesis and characterization of Fe-based amorphous composite by laser direct deposition, Surf. Coat. Technol. 239 (2014) 34–40, https://doi.org/10.1016/j.surfcoat.2013.11.013.
[45] N. Sohrabi, J. Jhabvala, G. Kurtuldu, R. Frison, A. Parrilli, M. Stoica, A. Neels, J. F. Löffler, R.E. Logé, Additive manufacturing of a precious bulk metallic glass, Appl. Mater. Today 24 (2021) 101080, https://doi.org/10.1016/j.apmt.2021.101080.
[46] G. Yang, X. Lin, F. Liu, Q. Hu, L. Ma, J. Li, W. Huang, Laser solid forming Zr-based bulk metallic glass, Intermetallics 22 (2012) 110–115, https://doi.org/10.1016/j.intermet.2011.10.008.
[47] Y.M. Zou, Y.S. Wu, K.F. Li, C.L. Tan, Z.G. Qiu, D.C. Zeng, Selective laser melting of crack-free Fe-based bulk metallic glass via chessboard scanning strategy, Mater. Lett. 272 (2020) 2–5, https://doi.org/10.1016/j.matlet.2020.127824.
[48] S. Venkataraman, K. Biswas, B.C. Wei, D.J. Sordelet, J. Eckert, On the fragility of Cu47Ti33Zr11Ni8Si1 metallic glass, J. Phys. D: Appl. Phys. 39 (12) (2006) 2600, https://doi.org/10.1088/0022-3727/39/12/020.
[49] J.A. Slotwinski, E.J. Garboczi, K.M. Hebenstreit, Porosity measurements and analysis for metal additive manufacturing process control, J. Res. Natl. Inst. Stand. Technol. 119 (2014) 494–528, https://doi.org/10.6028/jres.119.019.
[50] P. Wang, X. Tan, C. He, M.L.S. Nai, R. Huang, S.B. Tor, J. Wei, Scanning optical microscopy for porosity quantification of additively manufactured components, Addit. Manuf. 21 (2018) 350–358, https://doi.org/10.1016/j.addma.2018.03.019.
[51] P. Ferro, R. Meneghello, G. Savio, F. Berto, A modified volumetric energy density-based approach for porosity assessment in additive manufacturing process design, Int. J. Adv. Manuf. Technol. 110 (7) (2020) 1911–1921, https://doi.org/10.1007/s00170-020-05949-9.
[52] L. Wang, Y. Zhang, H.Y. Chia, W. Yan, Mechanism of keyhole pore formation in metal additive manufacturing, npj Comput. Mater. 8 (1) (2022) 22, https://doi.org/10.1038/s41524-022-00699-6.
[53] S.C. Glade, R. Busch, D.S. Lee, W.L. Johnson, R.K. Wunderlich, H.J. Fecht, Thermodynamics of Cu47Ti34Zr11Ni8, Zr52.5Cu17.9Ni14.6Al10Ti5 and Zr57Cu15.4Ni12.6Al10Nb5 bulk metallic glass forming alloys, J. Appl. Phys. 87 (10) (2000) 7242–7248, https://doi.org/10.1063/1.372975.
[54] D.V. Louzguine-Luzgin, T. Saito, J. Saida, A. Inoue, Thermal conductivity of metallic glassy alloys and its relationship to the glass forming ability and the observed cooling rates, J. Mater. Res. 23 (8) (2008) 2283–2287, https://doi.org/10.1557/jmr.2008.0286.
[55] L. Gargalis, J. Ye, M. Strantza, A. Rubenchik, J.W. Murray, A.T. Clare, I.A. Ashcroft, R. Hague, M.J. Matthews, Determining processing behaviour of pure Cu in laser powder bed fusion using direct micro-calorimetry, J. Mater. Process. Technol. 294 (2021) 117130, https://doi.org/10.1016/j.jmatprotec.2021.117130.
[56] B. Brandau, A. Da Silva, C. Wilsnack, F. Brueckner, A.F. Kaplan, Absorbance study of powder conditions for laser additive manufacturing, Mater. Des. 216 (2022) 110591, https://doi.org/10.1016/j.matdes.2022.110591.
[57] X. Gao, Z. Liu, J. Li, E. Liu, C. Yue, K. Zhao, G. Yang, Selective laser melting of CuZr-based metallic glass composites, Mater. Lett. 259 (2020) 126724, https://doi.org/10.1016/j.matlet.2019.126724.
[58] C.M. Grigorian, T.J. Rupert, Critical cooling rates for amorphous-to-ordered complexion transitions in Cu-rich nanocrystalline alloys, Acta Mater. 206 (2021) 116650, https://doi.org/10.1016/j.actamat.2021.116650.
[59] U. Scipioni Bertoli, G. Guss, S. Wu, M.J. Matthews, J.M. Schoenung, In-situ characterization of laser-powder interaction and cooling rates through high-speed imaging of powder bed fusion additive manufacturing, Mater. Des. 135 (2017) 385–396, https://doi.org/10.1016/j.matdes.2017.09.044.
[60] I. Okulov, I. Soldatov, I. Kaban, B. Sarac, F. Spieckermann, J. Eckert, Fabrication of metastable crystalline nanocomposites by flash annealing of Cu47.5Zr47.5Al5 metallic glass using joule heating, Nanomaterials 10 (1) (2020), https://doi.org/10.3390/nano10010084.
[61] R. Arroyave, T.W. Eagar, L. Kaufman, Thermodynamic assessment of the Cu-Ti-Zr system, J. Alloy. Compd. 351 (1-2) (2003) 158–170, https://doi.org/10.1016/S0925-8388(02)01035-6.
[62] A. Takeuchi, A. Inoue, Classification of Bulk Metallic Glasses by Atomic Size Difference, Heat of Mixing and Period of Constituent Elements and Its Application to Characterization of the Main Alloying Element, Mater. Trans. 46 (12) (2005) 2817–2829, https://doi.org/10.2320/matertrans.46.2817.
[63] Y.C. Kim, J.C. Lee, P.R. Cha, J.P. Ahn, E. Fleury, Enhanced glass forming ability and mechanical properties of new Cu-based bulk metallic glasses, Mater. Sci. Eng.: A 437 (2) (2006) 248–253, https://doi.org/10.1016/j.msea.2006.07.141.
[64] C. Li, J. Saida, M. Kiminami, A. Inoue, Dynamic crystallization process in a supercooled liquid region of Cu40Ti30Ni15Zr10Sn5 amorphous alloy, J. Non-Cryst. Solids 261 (1) (2000) 108–114, https://doi.org/10.1016/S0022-3093(99)00661-4.
[65] W.L. Johnson, J.H. Na, M.D. Demetriou, Quantifying the origin of metallic glass formation, Nat. Commun. 7 (1) (2016) 10313, https://doi.org/10.1038/ncomms10313.
[66] I.V. Okulov, I.V. Soldatov, M.F. Sarmanova, I. Kaban, T. Gemming, K. Edström, J. Eckert, Flash Joule heating for ductilization of metallic glasses, Nat. Commun. 6 (2015) 1–6, https://doi.org/10.1038/ncomms8932.
[67] M. Rappaz, J.A. Dantzig, Solidification, EPFL Press, 2009. https://books.google.de/books?hl=de&lr=&id=bl-5L7cL0zAC&oi=fnd&pg=PR5&dq=M.+Rappaz,+J.+A.+Dantzig,+Solidification,+EPFL+Press,+2009.&ots=gFD_dW-XLc&sig=apAV-gB_eDrk9v9GDRJRpJz62TI#v=onepage&q=M.%20Rappaz%2C%20J.%20A.%20Dantzig%2C%20Solidification%2C%20EPFL%20Press%2C%202009.&f=false.
[68] G. Gottstein, Phys. Found. Mater. Sci. (2004), https://doi.org/10.1007/978-3-662-09291-0.
[69] E.S. Park, H.J. Chang, D.H. Kim, Improvement of glass-forming ability and phase separation in Cu-Ti-rich Cu-Ti-Zr-Ni-Si bulk metallic glasses, J. Alloy. Compd. 504 (SUPPL 1 (2010) S27–S30, https://doi.org/10.1016/j.jallcom.2010.04.129.

[70] Y.J. Yang, R. Zhou, S.D. Wei, D.Y. Liu, H.L. Xu, S.L. Li, Microstructural evolution of slowly solidified Cu-Ti-Zr-Ni amorphous alloy, J. Non-Cryst. Solids 357 (6) (2011) 1516–1521, https://doi.org/10.1016/j.jnoncrysol.2010.12.043.
[71] J. Lindwall, A. Lundbäck, J.J. Marattukalam, A. Ericsson, Virtual development of process parameters for bulk metallic glass formation in laser-based powder bed fusion, Materials (2022), https://doi.org/10.3390/ma15020450.
[72] N. Ciftci, Cooling strategies for the atomization of glass-forming alloys, PHD Thesis (June) 153.10.26092/elib/84.
[73] H.Y. Jung, S.J. Choi, K.G. Prashanth, M. Stoica, S. Scudino, S. Yi, U. Kühn, D. H. Kim, K.B. Kim, J. Eckert, Fabrication of Fe-based bulk metallic glass by selective laser melting: a parameter study, Mater. Des. 86 (2015) 703–708, https://doi.org/10.1016/j.matdes.2015.07.145.
[74] X.D. Nong, X.L. Zhou, Y.X. Ren, Fabrication and characterization of Fe-based metallic glasses by selective laser melting, Opt. Laser Technol. 109 (2019) 20–26, https://doi.org/10.1016/j.optlastec.2018.07.059.